

Evaluating the Electrochemical Behavior of Friction Stir-Welded AA2219-O Alloy Joint in 3.5% NaCl Solution

F.A. Ghauri, K.M. Deen, A. Farooq, M. Afzal, and A. Ahmad

(Submitted September 29, 2017; in revised form April 9, 2018; published online June 18, 2018)

Single-pass friction stir welding of AA2219-O aluminum alloy was carried out at high rotation speed (1180 rpm), and transverse travel rate of 33.5 mm/min was selected. The microstructural, mechanical and electrochemical characteristics of the weldment are investigated in this study. The high rotational tool speed resulted in a less uniform distribution of the intermetallic θ -phase (CuAl_2) in the thermo-mechanically affected zone (TMAZ) than in the weld nugget zone (WNZ). The higher transfer coefficient and lower charge transfer resistance ($R_{ct} + R_\theta$) were observed in case of TMAZ as evaluated from potentiodynamic polarization and impedance spectroscopy, respectively. These results confirmed that microstructural variations could deteriorate the electrochemical performance of the weldment. TMAZ provided the least corrosion resistance than the base metal (BM) and WNZ due to the high concentration of cathodic intermetallic particles and possibly due to the large mechanical distortion of the grain structure.

Keywords electrochemical, impedance spectroscopy, friction stir welding, polarization

1. Introduction

The solid-state joining process, i.e., friction stir welding (FSW) of Al-Cu alloys, is always preferred to avoid microstructural inhomogeneity and to achieve high mechanical and electrochemical performance compared to fusion welding processes. During FSW, the heat produced by the rotating tool is constrained within a small region to facilitate the softening of alloy and strong weld is produced through inter-diffusion of metal atoms across the weld joint. It is also well documented that maximum heat within the weld nugget zone (WNZ) promotes the formation of equiaxed and recrystallized grain structure. However, adjacent to the WNZ, in the thermo-mechanically affected zone (TMAZ), the severe microstructural distortion is always induced by the stirring action of the tool pin (Ref 1-7).

It has been stated that the FSW provides superior hardness and mechanical strength than other conventional fusion welding processes (Ref 8). During FSW process, the heat generation could affect the microstructure and would produce three distinct zones, WNZ, heat-affected zone (HAZ), TMAZ and unaffected base metal (BM). The microstructural modifications and

residual stresses introduced by FSW will also govern to the corrosion response of weldment. It has been identified that the FSW will produce residual stresses during the joining of aluminum sheets which could modify the mechanical and corrosion properties (Ref 9). Hatamleh et al. (Ref 10) reported that high residual stresses were obtained in TMAZ and WNZ due to FSW of aluminum alloys. Farajkhah et al. (Ref 11) also pointed out that the friction welding may induce residual stresses which may vary with welding parameters.

Furthermore, the corrosion rate of the weldment and the location of the corrosion attack depend on the composition of alloy and welding parameters. Wadeson et al. (Ref 12) reported that in case of AA7108 alloy the region near the edge of TMAZ was more prone to corrosion attack. In another study by Kang et al. (Ref 13) evaluated that after FSW of AA2024, the weld center represented higher corrosion rate than BM and TMAZ.

In various studies, the effect of FSW on the thermal (Ref 14, 15), microstructural (Ref 16, 17), material flow characteristics (Ref 18, 19), electrochemical behavior (Ref 12, 20, 21) and mechanical properties (Ref 22, 23) of the 7xxx, 2xxx and 6xxx aluminum alloys has been discussed. AA2219 alloy has specific use in the aerospace and defense-related applications due to its good strength-to-weight ratio, excellent mechanical properties in cryogenic conditions and better weld-ability than 6xxx and 7xxx Al alloys. In AA2219 alloy, the intermetallic ' θ ' phase (CuAl_2) is responsible for its good mechanical strength. However, the morphology and distribution of this phase could significantly influence the corrosion properties. It is possible that this phase could form localized galvanic couple with the surrounding Al matrix, hence leading to localized attack. The morphology, density and electronegativity difference between intermetallic phase CuAl_2 and Al matrix regulates the corrosion performance of AA2219 alloy. Jariyaboon et al. (Ref 20) studied the effect of welding parameters (travel and rotational speed) on the corrosion behavior of AA 2024-T351 in the naturally aerated 0.1 M NaCl solution. They reported that location of the corrosion attack in the weldment depends mainly on the rotational speed. Furthermore, the WNZ showed enhanced susceptibility to inter-granular attack at low rotational speed (215 rpm) compared to BM and TMAZ. Surekha et al.

F.A. Ghauri and A. Ahmad, Department of Metallurgical and Materials Engineering, University of Engineering and Technology, Lahore 54890, Pakistan; K.M. Deen, Department of Materials Engineering, The University of British Columbia, Stores Road, Vancouver, BC V6T 1Z4, Canada; and Corrosion Control Research Cell, Department of Metallurgy and Materials Engineering, CEET, University of the Punjab, Lahore 54590, Pakistan; A. Farooq, Corrosion Control Research Cell, Department of Metallurgy and Materials Engineering, CEET, University of the Punjab, Lahore 54590, Pakistan; and M. Afzal, NINVEST, NCP Complex, Quaid-e-Azam University, Islamabad, Pakistan. Contact e-mail: kmdeem.ceet@pu.edu.pk.

(Ref 24) also reported that the corrosion resistance of the stirred zone in 3.5% NaCl solution was much higher at high rotation speed of tool during FSW. They deduced that the possible reason for the improved corrosion resistance was due to the presence of low concentration of Al_2Cu particles in WNZ. Xu et al. (Ref 25) studied the corrosion behavior of AA2219-O alloy's welded joint in the alkaline solution and reported that high rotational speed during FSW greatly increased the corrosion resistance of WNZ. In another study about the FSW of AA2024-T3 alloy, Bousquet et al. (Ref 26) identified the HAZ as the most sensitive region toward corrosion due to the presence of large amount of second-phase particles. They also suggested that the corrosion tendency of the weldment greatly depends on the morphology and density of intermetallic phase in the Al matrix. Additionally, Rao et al. (Ref 27) investigated the influence of tool pin on the heat generation and pitting corrosion resistance of AA2219 alloy. They concluded that large amount of heat generation during FSW could be beneficial to dissolve Al_2Cu particles and to improve corrosion resistance.

It is perceived from the literature that high rotation speed of the tool during FSW of AA2219 alloy could be beneficial for better corrosion properties. As discussed above, some studies state the improvement in the corrosion resistance of WNZ and some negate the deleterious effects of tool rotational speed on the development of CuAl_2 phase. In the available literature, the large variation in the corrosion results is possible due to certain differences in the chemical composition and considerably to the applied welding parameters. In this study, we investigated the corrosion tendency of different regions formed during FSW at high rotational speed (1180 rpm). It is considered that large amount of heat generation during welding process could facilitate in situ homogenization of the microstructure specially, in the WNZ of alloy AA 2219-O. Furthermore, there is limited data available about the electrochemical response of AA 2219-O weldments in the saline environment. Potentiodynamic polarization and impedance spectroscopy tests were performed to investigate the corrosion behavior of weldment in relation to the microstructural features.

2. Experimental Work

Four-mm-thick plates of alloy AA2219-O with the nominal composition [Cu (6.27), Mn (0.29), Fe (0.15), Ti (0.07), V (0.13), Si (0.05), Zr (0.14) in wt.%] were joined by FSW process. Briefly, rectangular aluminum plates (270 mm \times 50 mm) were cut and longitudinal butt-welded joint was prepared by using FSW machine (FSW Technology Co, Ltd, Beijing, China). The plates were tightly fixed on the milling machine table to avoid vibration and movement which may result from the friction produced during the welding process. A 5-mm-diameter and 3.6-mm-long carbon steel threaded pin with a flat shoulder of 15 mm was used for the welding. To achieve uniform distribution of intermetallic (CuAl_2) phase, single-pass FSW was carried out at high rotational tool speed (1180 rpm) and transverse speed of (33.5 mm/min) was adjusted.

To reveal the microstructural variation during welding, the samples from each BM, TMAZ, WNZ and HAZ were cut with a precision wire cutter without heating the samples, ground on silicon carbide papers, sequentially from 120 to 2500 grit size followed by polishing with a diamond paste (1 μm). The

mirror-like polished surfaces were produced and etched in the Keller's reagent (150 ml H_2O , 3 ml HNO_3 , 6 ml HCl and 6 ml HF) to reveal microstructural features through an optical microscope (Leica, Wetzlar, Germany) and scanning electron microscope (SEM).

Tensile samples were cut by following the ASTM E8 standard. Tensile tests were conducted at room temperature by using the universal tensile testing machine (Instron, Norwood, MA) and 0.1 mm/mm/min strain rate was selected to measure the yield and tensile strength. After tensile testing, the morphology of the fractured surface was also examined through scanning electron microscopy. Vickers micro-hardness (Qualitest, USA) was measured across the weld zone under 2.942 N load for 6-s dwell period.

The electrochemical behavior of these samples was determined by potentiodynamic polarization and electrochemical impedance spectroscopy (EIS) tests by using PC14/750 potentiostat (Gamry Instruments, Inc. USA). The polarization and impedance data were analyzed using Echem analyst software version 5.68. For electrochemical testing 1 cm^2 samples were cut from each BM, HAZ, TMAZ and WNZ of the weld joint. After FSW, both sides across the weld represented asymmetrical features due to directional tool rotation. The advancing side (AS) is the direction of the tool rotation and the retreating side (RS) represent the weld region following tool movement. The sample for TMAZ electrochemical testing was taken from the AS side, which usually experiences severe thermal and mechanical stresses compared to RS. The electrodes for the corrosion testing were prepared by attaching a glass-encased wire at the back face (opposite to the exposed surface) of the samples for electrical connection and mounted in polyester resin. The exposed surface of each sample was ground on SiC papers up to 1000 grit size prior to cleaning and electrochemical testing. These mounted and polished samples were then used as working electrodes in a three-electrode cell. The counter and reference electrodes used were graphite rod and saturated calomel (SCE), respectively. The de-aerated 3.5% NaCl solution was sparged with nitrogen gas for 1800 s before executing the electrochemical tests.

The corrosion potential of the samples was measured until stable with a variation of 0–2 mV in at least 3600 s. Potentiodynamic polarization tests were carried out at a scan rate of 5 mV/s from an initial potential of -0.5 V versus OCP to a final potential of +1.5 V (versus OCP). The impedance spectra were obtained by exerting ± 10 mV_(rms) AC potential amplitude over OCP and spectra were obtained within 100 kHz to 0.01 Hz frequency range.

3. Results and Discussion

3.1 Microstructural Analysis

Figure 1 represents the microstructures of different zones produced after welding of AA 2219-O alloy. Within the weld joint, the microstructural variation can be distinguished and termed as BM, WNZ, TMAZ and the HAZ, respectively, as mentioned by Janjić et al. (Ref 28). It was observed that the microstructure of AA 2219-O (BM) [Fig. 1(a)] was composed of a eutectic phase containing randomly distributed fine ' θ ' phase (CuAl_2 intermetallic precipitates) in 'Al'-rich α -solid solution matrix phase. Also, the pro-eutectic α -phase could be observed along the precipitate. The regular shape CuAl_2

intermetallic precipitates are also evident in Fig. 1(a). In FSW joints, the region adjacent to the weld, designated as TMAZ, also experiences severe plastic deformation and temperature excursion but the heat conducted in this region was insufficient to initiate recrystallization. This has distorted the grain structure and has affected the distribution of the ' θ ' phase as shown in Fig. 1(b).

The WNZ was the region where maximum heat is generated due to the high rotational speed of the advancing tool. In this region, the microstructure was composed of equiaxed grains due to higher recrystallization tendency and relatively uniform distribution of intermetallic precipitates. The quasi-equilibrium thermal state and mechanical stirring during welding process have not dissolved the CuAl_2 precipitates (θ -phase) in solid solution but have affected considerably their geometry and distribution. Relatively small and uniformly distributed precipitates can be observed in Fig. 1(c). The recrystallization and redistribution of ' θ ' phase are expected due to vigorous heat generation and thermo-mechanical stresses induced by high rotational speed (1180 rpm) of the tool (Ref 29).

Away from the TMAZ, the small temperature amplitude produced negligible influence on the microstructure in the very narrow region designated as 'HAZ.' In our case, the microstructure in this zone was almost similar to the BM zone due to relatively negligible thermo-mechanical forces as depicted in Fig. 1(d). Therefore, this region was not considered for further characterization.

Figure 2(a), (b) and (c) shows the high-resolution images of BM, TMAZ and WNZ samples obtained from scanning electron microscope (SEM). It was revealed that the TMAZ had the localized distribution of the second-phase (θ) CuAl_2 particles mostly agglomerated at the grain boundaries. These precipitates (10–1 μm) were also present within the grains of α -Al matrix. Additionally, certain CuAl_2 particles were

elongated due to stirring action of the tool and the temperature in this zone was insufficient to completely dissolve these particles. Bousquet et al. (Ref 26) described the similar features of TMAZ under applied conditions. On the other hand, the relatively uniform distribution of second-phase particles was observed in the WNZ and their size was in the range of ~ 6 –1 μm due to combined action of stirring and heat generation by the pin and shoulder during FSW [Fig. 1(c), and 2(c)]. The overall composition of the alloy as determined from the EDX analysis confirmed the presence of Cu (~ 6.2 wt.%) as major alloying elements. The point EDX analysis was used to estimate the average composition of the precipitates in the BM, TMAZ and WNZ. These results validate the molar ratio of 1.98 [Al (moles): Cu (moles)] which was in agreement with the presence of CuAl_2 phase in α -Al matrix [Fig. 2(a), (b) and (c)].

Figure 2(d) presents the XRD patterns of BM, TMAZ and WNZ. The diffraction patterns of the BM, TMAZ and WNZ represented the major peaks of α -Al phase at 38.7° , 44.9° , 65.4° , 78.5° and 82.7° which corresponded to the (111), (200), (220), (311) and (222) planes, respectively, according to PDF # 04-0787 reference pattern. However, some additional diffraction signals originated at 42.97° , 48.17° and 83.06° exhibited by the (112), (202) and (420) planes, respectively, also assured the existence of CuAl_2 phase (PDF # 25-0012) in the Al matrix. Additionally, it can be observed that the diffraction intensity from the (111) major plane in the BM decreased sequentially in TMAZ and WNZ. The dominant (200) plane in the TMAZ and WNZ could be associated with the thermo-mechanical effects produced during FSW process.

3.2 Mechanical Properties

The tensile tests for the base and friction stir-welded specimen were conducted to evaluate joint efficiency (the ratio

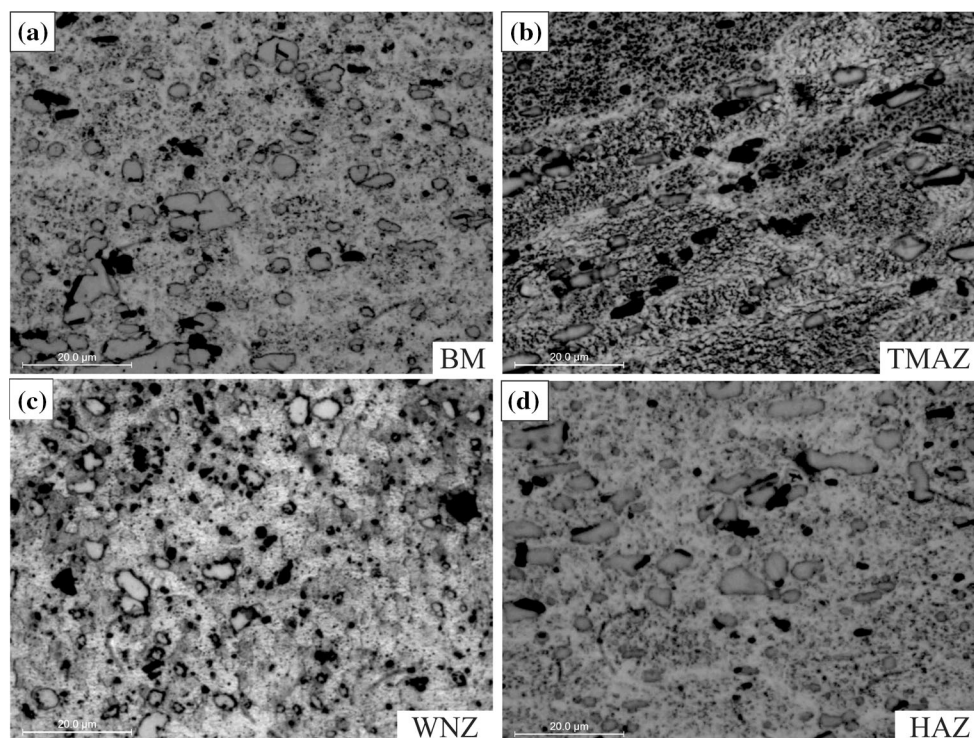


Fig. 1 Optical micrographs showing the microstructures of various zones developed during friction stirred welding of AA-2219-O alloy

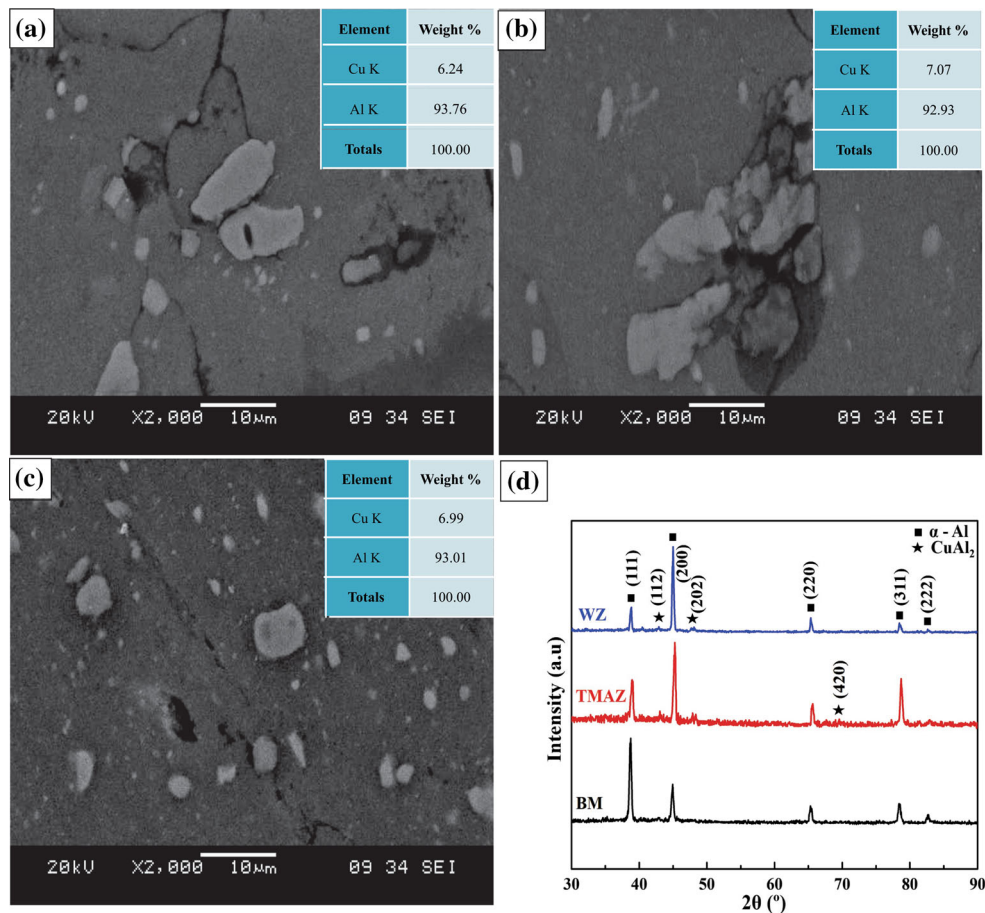


Fig. 2 SEM images of the (a) BM, (b) TMAZ, (c) WNZ and (d) XRD patterns represent the diffraction peaks corresponding to α -Al matrix and CuAl_2 phase

of tensile strength of the welded joint to tensile strength of the un-welded BM). Under applied welding conditions, a slight decrease in tensile strength of the welded sample (160 ± 0.30 MPa) compared to the un-welded BM (166 ± 0.25 MPa) resulted in a joint efficiency of 96.38%. Similarly, 5% decrease in elongation of the welded sample and increase in yield strength from 80 ± 0.15 MPa (for BM) to 89 ± 0.23 MPa (for welded samples) corresponded to the distorted grain structure in the TMAZ. The intense thermo-mechanical stresses at high rotational and low transverse speed promoted strain hardening of the grain structure, which led to a slight increase in the yield strength of the welded sample (Ref 30). The low tensile strength and decrease in % elongation were also attributed to plastic deformation in the TMAZ during welding. Xu et al. (Ref 31) also reported better joint efficiency and decrease in % elongation at high rotational speed during FSW of AA2219-O thick plate. Due to the difference in the welding parameters, it is difficult to make a direct comparison in this case. However, the tensile strength and % elongation of the weldment as claimed in this study were promising in order to support the reported values by Chen et al. (Ref 32). According to this study, at tool rotation speed of 800 rpm the joint efficiency of the AA2219-O weldment was $\sim 60\%$. Whereas, the high joint efficiency in our case was related with the in situ homogenization of the welded joint obtained at relatively higher tool speed.

The fracture surface of the welded sample obtained after tensile tests is presented in [Fig. 3(a), and (b)]. The sample was fractured from the BM adjacent to the TMAZ where the micro-hardness was relatively lower than for the WNZ. The results were similar to those reported by Liu et al. (Ref 33). A typical ductile fracture surface was revealed containing trans-granular dimple-like features. The edges of these shallow dimples were deformed representing significant plastic deformation through the alpha matrix phase as shown in the inset of Fig. 2(b). Within the dimples, the presence of intermetallic precipitates corresponded to the nucleation and coalescence of micro-voids at the interface of soft α -Al (matrix) and hard CuAl_2 (θ -phase) (Ref 34, 35).

Figure 3(c) represents the micro-hardness profile of welded sample across the weld line. With reference to the weld centerline, the micro-hardness varied from a maximum of 67.6 ± 0.3 HV at the WNZ to 51.43 ± 0.5 HV on both sides of the WNZ within the BM. The relatively fine recrystallized grain structure and relatively uniform distribution of CuAl_2 precipitates formed in the weld zone during a vigorous thermo-mechanical cycle could increase the hardness of the WNZ as observed in the profile. The hardness values were nearly symmetrical at either side of the weld line. Liechty et al. (Ref 30) reported the asymmetrical profile across the weld centerline at low rpm caused by non-uniform plastic flow behavior of the weld metal due to the tool pin movement at the advancing side of the weld.

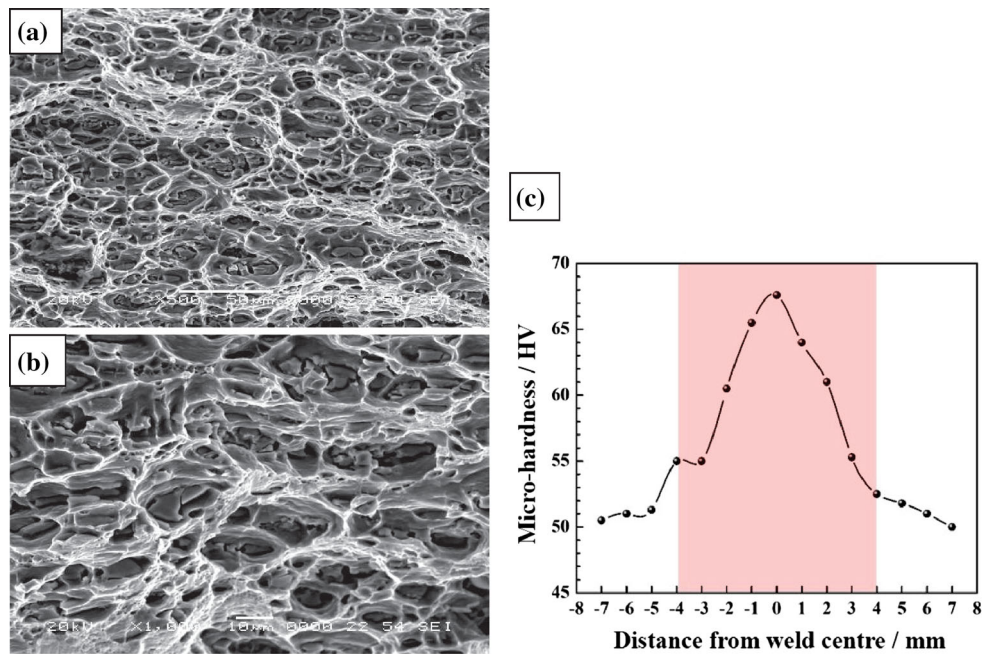


Fig. 3 Fracture surface of AA 2219-O specimen after tensile test (a) low magnification, (b) high magnification and (c) hardness profile of weldment within base metal both at the advancing (AS) the retreating side (RS) of the WNZ

3.3 Electrochemical Study

The specimens for electrochemical testing were cut from BM, WNZ and TMAZ after macro-etching of the weld joint to identify different zones. The corrosion tendency and kinetic behavior of these separate zones were investigated from potentiodynamic polarization.

Al and its alloys in the aqueous medium quickly form a passive film which is considered to be compact, inert and limit the dissolution of bulk metal. But in the aggressive environment, i.e., in chloride containing solution, the localized corrosion of aluminum alloys has been reported in the literature. There are several mechanisms which describe the dissolution of the passive film on aluminum alloys in the presence of chloride ions. These include the breakdown of the passive film by ingress of anions into the Al_2O_3 lattice or penetration of Cl^- ion through the pores and micro-defects and field-assisted competitive adsorption of either Cl^- or OH^- within the passive films (Ref 36, 37).

The potentiodynamic trends are shown in Fig. 4. The large cathodic polarization in case of BM and WNZ corresponded to the limited reduction in water (Reaction 1). However, during cathodic polarization, the relatively larger current response by the TMAZ sample was associated with the presence of active sites within the microstructure which may catalyze the cathodic reactions. In order to quantify the corrosion rate and for the calculation of Tafel parameters, the high field potential region was selected ($> \pm 0.1$ VSCE) for interpolation of the anodic and cathodic polarization curves in the Tafel region as shown in Fig. 4. The Tafel slopes for BM, TMAZ and WNZ within this region and electrochemical behavior at low potential within $0.1\text{VSCE} < E - E_{\text{corr}} < 0.1\text{VSCE}$ range could be used to predict the mechanism of corrosion reaction mechanisms. It was found that the cathodic Tafel slope (bc) of BM, WNZ and TMAZ specimens was 0.584, 0.115 and 0.820 V/decade, respectively. On the basis of 'bc' values, it could be estimated

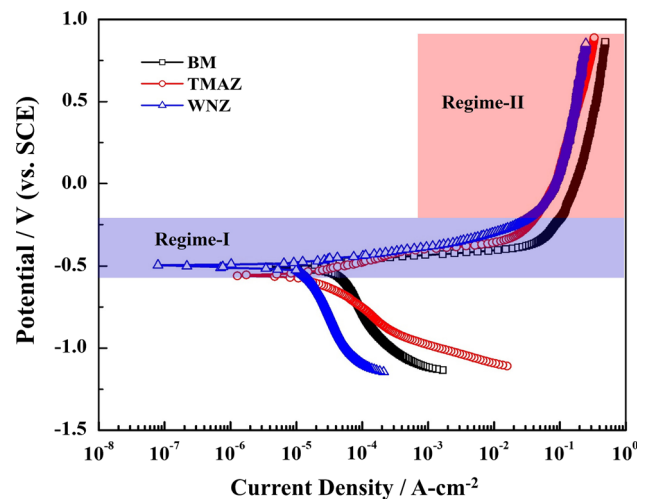
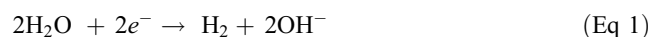
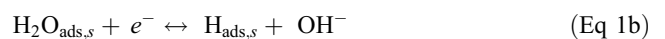


Fig. 4 Potentiodynamic polarization scans of AA 2219-O weldment in 3.5% NaCl solution

that the electrochemical reaction over BM and WNZ may be controlled by the rate determining intermediate reactions possibly related to the reduction in water at the surface (Ref 36) (as given in Reactions 1a-1d).



This reaction can be further broken down into the following steps





or



The Al_2O_3 passive film has a strong affinity for hydration when exposed to aqueous media (Reaction 1a). The non-uniform or defective passive film over the TMAZ could develop due to the presence of high concentration of $CuAl_2$ (θ phase) which may act as local cathodic sites for hydrogen evolution as predicted from the low 'bc' value. The adsorbed hydrogen ' $H_{ads,s}$ ' species could possibly follow either step reaction 1c or 1d as a function of film continuity and the catalytic activity of the intermetallic θ phase (Ref 38). Birbilis et al. (Ref 39) also reported that $CuAl_2$ intermetallic phase presented relatively more noble potential than Al in 0.6 M chloride solution. This could also be evaluated from the large charge transfer coefficient value of TMAZ (Fig. 5) as calculated from the 'bc.' This was attributed to the larger electrochemical activity of TMAZ for cathodic reaction which can be directly related to the presence of the large concentration of θ phase. During welding, the generation of high mechanical stresses in the TMAZ caused severe distortion and disturbed the continuity of the passive film due to precipitation and agglomeration of secondary particles. Compared to WNZ, the low-temperature excursion in this zone could also hinder the stabilization (recrystallization) of microstructure (Ref 29).

The anodic polarization curves depicted the two differentiable regimes, i.e., high current response at low applied field and potential independent limiting current density at large

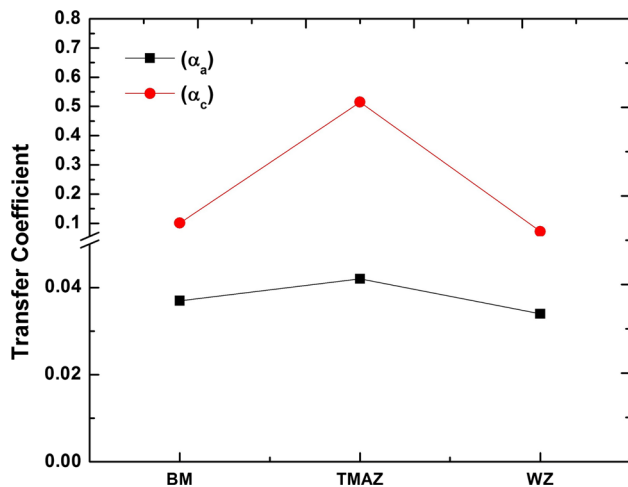
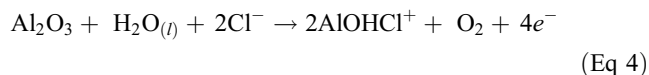
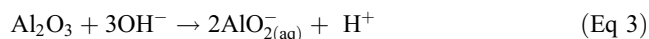
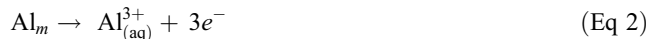


Fig. 5 Variation of anodic and cathodic transfer coefficient calculated from the slopes of polarization curves in the Tafel region; $a_x = \frac{2.303 RT}{\beta_x F}$ (where ' β_x ' is the Tafel slope and ' α_x ' is the transfer coefficient, ' F ' is the Faraday's constant and ' R ' is universal gas constant. ' x ' in the subscript represents the anodic or cathodic)

potential. The low over-potential within regime-I was attributed to the stripping of adsorbed $H_2O_{ads,s}$ and uniform dissolution of the Al_2O_3 passive film by the competitive action of OH^- and Cl^- ions present in the electrolyte. Nguyen et al. (Ref 38) proposed a four-step reaction mechanism for pitting and dissolution of passive film on aluminum: (1) adsorption of anions within the film (2) reaction with Al^{3+} in the Al_2O_3 crystal lattice, (3) uniform thinning of passive film and (4) localized reactions within the defects by forming soluble complexes. Following this proposed theory for uniform and thick passive film, the dissolution step 1 and 2 would be controlled by the migration of OH^- and Cl^- anions toward the oxide/metal interface and may interact with Al^{3+} ions at the oxide/solution interface.

Within regime-I, the larger current response was attributed to the dissolution of Al matrix phase (Reaction 2) and hydrolysis of the Al_2O_3 passive film (Reaction 3). The high concentration of Cl^- ions in the electrolyte could also depolarize the surface by forming complexes with the oxide film (Reaction 4). The proposed mechanism for preferential dissolution of Al compared to the second-phase particles and thinning of the passive film in neutral 3.5% NaCl solution has been validated by the kinetic parameters and was in support of the model proposed by Foroulis et al. (Ref 40).



The anodic reactions at the surface of AA 2219-O weldment strongly depend on the microstructure, i.e., uniformity of the passive film, distribution and morphology of the second-phase intermetallic (θ) $CuAl_2$ particles within the α -matrix. Xu et al. (Ref 41) observed that the shape and distribution of $CuAl_2$ (θ -phase) within the α -matrix phase has a strong influence on the electrochemical dissolution of friction stir-welded joints of AA2219-O.

At high anodic potential (regime-II), the large limiting current density was observed in case of BM compared to TMAZ and WNZ. This may be attributed to the non-homogeneity in the microstructure and presence of large size intermetallic particles. The localized dissolution of Al matrix at the interface of these particles could be estimated from the large current density. This could be explained by considering the mechanism as given in Reactions 2, 2a, 2b. At higher anodic potential, the competitive reactions hydrolysis (Reaction 2a) and chloride-assisted dissolution (Reaction 2b) would strongly

Table 1 The parameters calculated by fitting the experimental impedance spectra with the EEC model

Speciman	$Y_0, \mu S.S^{\frac{1}{n}}.cm^{-2}$	n	$R_{ct}, \Omega.cm^2$	$R_e, \Omega.cm^2$	$C_e, \mu F.cm^{-2}$
BM	316.13	0.785	271.30	566.0	92.85
TMAZ	533.08	0.733	129.91	519.5	75.78
WNZ	702.62	0.670	26.56	964.5	70.57

depend on the continuity of the Al_2O_3 passive film. The localized dissolution of an active site within a passive film defect is accelerated by the depolarization effect of chloride (Cl^-) ions and by the formation of water-soluble metal chloride species, i.e., AlOHCl^+ and AlO_2^- under applied conditions (via Reaction 2b, 3 and 4, respectively). These reactions are strongly pH dependent and would occur under high applied potential (within region-II). It is, therefore, commented that dissolution of the uniform passive film is controlled by the strong hydration characteristics than chloride-assisted attack (Ref 42).

The hydration of the passive film at low anodic potential and under neutral pH condition will decrease the chloride-assisted dissolution of WNZ. Jariyaboon et al. (Ref 20) also reported that the tool rotational speed strongly influenced the electrochemical behavior of the weldment and deduced that WNZ would experience limited corrosion attack at higher tool rotational speed than TMAZ and vice versa at lower speed due to microstructural variations.

Thus, the electrochemical stability of BM, TMAZ and WNZ strongly depends on the microstructural characteristics such as distribution of the cathodic ' θ ' particles and the environmental conditions. The higher anodic Tafel slope (b_a) of BM and WNZ compared to TMAZ registered low transfer coefficients (Fig. 5). Compared to cathodic transfer coefficient ' α_c ', the lower anodic transfer coefficient ' α_a ' calculated from polarization curve suggested the dominance of hydration (by OH^-) (Reaction 2a) over dissolution (by Cl^-) (Reaction 2b) at the oxide/solution interface. The relatively higher α_a for TMAZ compared to BM and WZ also corresponded to the simultaneous occurrence of reactions 2 and 4 at the defect (local active site) and over the passive film.

The limiting anodic current density values registered by BM ($28.2 \mu\text{A}/\text{cm}^2$), TMAZ ($13.8 \mu\text{A}/\text{cm}^2$) and WNZ ($1.02 \mu\text{A}/\text{cm}^2$) were relatively lower than those reported by Xu et al. (Ref 41) for a weldment produced at low tool rotational speed in 3.5% NaCl solution. Also, the higher current density observed for the BM than TMAZ, WNZ could be beneficial to avoid localized weld attack. An order of magnitude lower anodic current density and relatively smaller corrosion current density exhibited by WNZ was in agreement with the findings by Surekha et al. (Ref 24). In contrast, attributing to the significant difference in welding parameters, the lower corrosion current density was registered by TMAZ compared to WNZ as described in another report (Ref 43).

In order to explain the interfacial electrochemical characteristics of BM, WNZ and TMAZ, the EIS spectra were also obtained at OCP (open-circuit potential). The potential was stabilized prior to applying small alternating potential amplitude ($10 \text{ mV}_{\text{rms}}$) and by varying the frequency from 100 kHz to 0.01 Hz. It was determined from the polarization tests that large increase in current was observed in regime-I (at low applied potential beyond $E_{\text{corr}}/\text{OCP}$) in case of all BM, TMAZ and WNZ. It is, therefore, the small potential amplitude over the OCP would determine the electrochemical activity of the reversible reactions occurring at the surface. The Nyquist plots (as shown in Fig. 6) for each BM, TMAZ and WNZ, were simulated with the equivalent electrical circuit (EEC) model (Fig. 7). The quantitative kinetic information obtained after fitting the experimental impedance data with the given EEC model is provided in Table 1. The ' R_s ', ' R_{ct} ', ' Y_0 ' and ' n ' are denoted as solution resistance, charge transfer resistance, admittance and relaxation coefficient for double layer, respec-

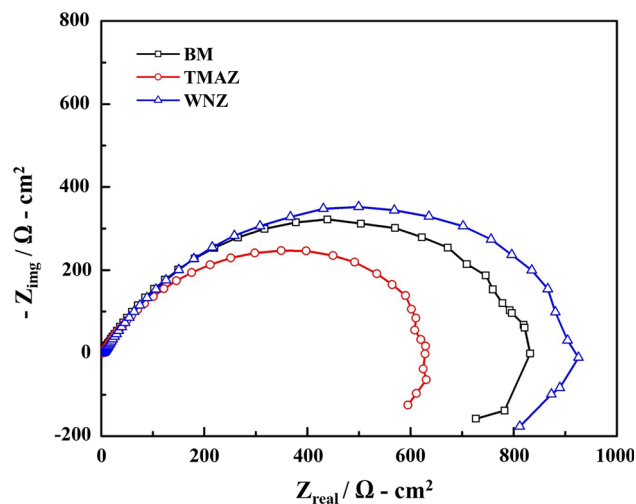


Fig. 6 Impedance spectra (Nyquist plots) for AA2219-O alloy weldment in 3.5% NaCl solution obtained at 0 V vs. OCP

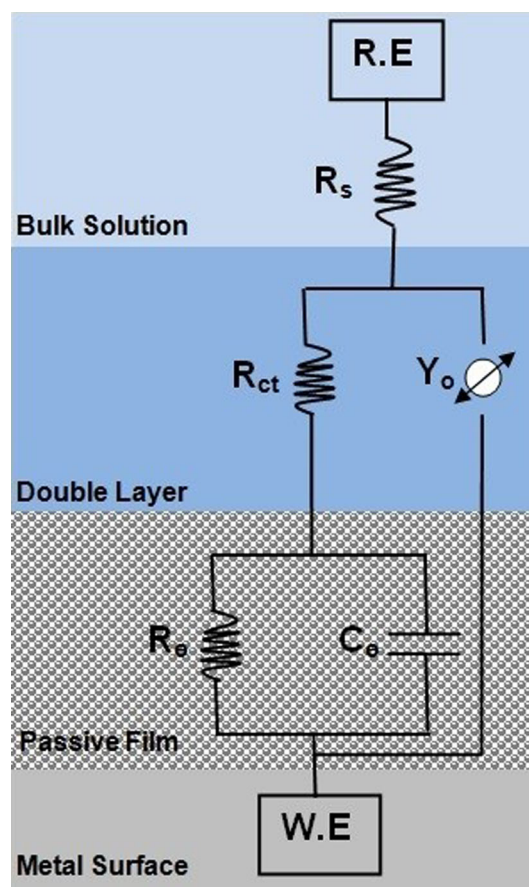


Fig. 7 The equivalent electrical circuit (EEC) model used to simulate the experimental spectra with the physical system and to evaluate quantitative information

tively. The ' C_0 ' and ' R_0 ' in the EEC model were associated with the passive film and to the adsorption/desorption behavior of the intermediate species.

The relatively depressed semicircle at high frequency was related to the double-layer charging and charge transfer resistance for the electrochemical reactions at the electrolyte/

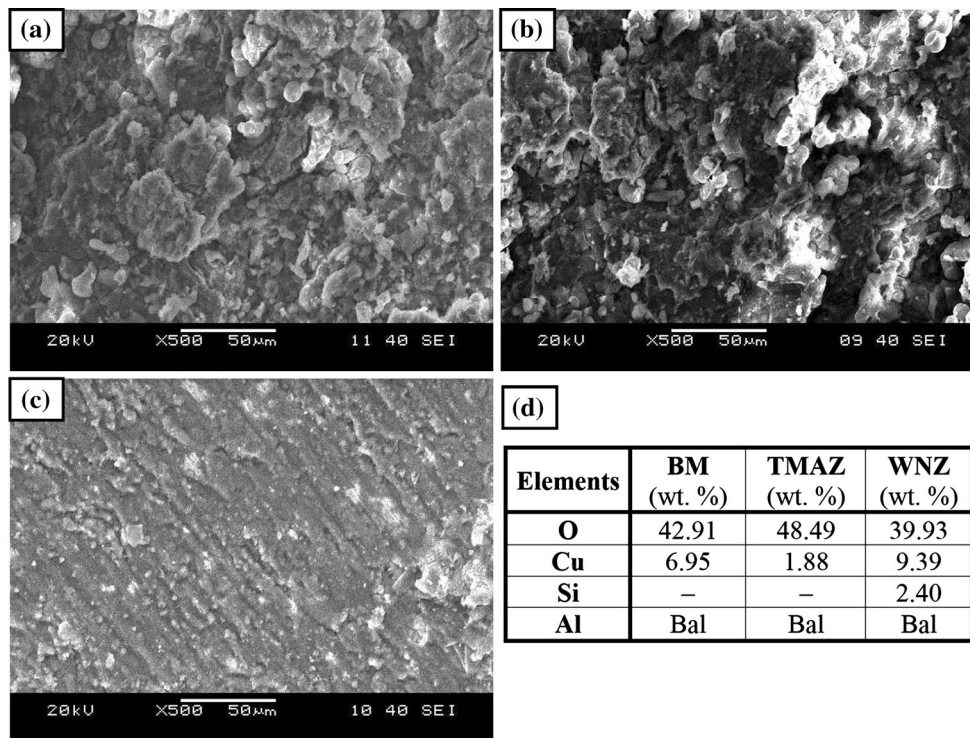
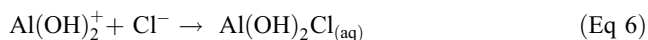


Fig. 8 The micrographs showing the surface of (a) BM, (b) TMAZ, (c) WNZ after exposure to 3.5% NaCl solution and (d) EDX analysis of the weld zones

oxide film interface, whereas the low-frequency impedance response was affiliated with the distribution of adsorbed species and to the charge transfer associated with the desorption of intermediate species from the surface. The electrochemical reactions at the surface of the passive film were controlled by the individual contribution of R_{ct} and R_0 . It was observed that total resistance ($R_{ct} + R_0$) for both BM and WNZ was higher than TMAZ.

The localized Reactions (2 and 2b) will take place preferentially at the active sites, i.e., at the edges of α -matrix/ θ -phase or at the vicinity of defects within the passive film. As a result, the ionization of hydrated oxide film will occur and basic aluminum chloride salt is formed according to Reactions 5 and 6, respectively (Ref 1, 42).



The WNZ showed lower R_{ct} and smaller relaxation coefficient (n) corresponded to the formation of OH^- and H_{ads} by the reduction of $(\text{H}_2\text{O})_{\text{ads}}$ (Reaction 1b) species. But the dissolution of the passive film on WNZ was limited due to hydrolysis of cationic species, i.e., Al^{3+} (Reaction 2a) and Al(OH)_2^+ ions (reverse of Reaction 5). This behavior was confirmed by the higher ' R_0 ' ($964.5 \Omega \cdot \text{cm}^2$) 'adsorption of H_{ads} ' and admittance (Y_0) (formation of Al(OH)_3), respectively. Hence, the effect of chloride on the dissolution of the passive film (Reaction 6) is reduced. The relatively lower R_0 ($519.5 \Omega \cdot \text{cm}^2$) represented by TMAZ and higher transfer coefficient (α_a, α_c) also confirmed the possibility of favorable water reduction (Reaction 1c) and chloride-assisted localized dissolution (Reactions 2b, 4 and/or 6) Reactions. The high ' C_0 ' adsorption capacitance by the BM can be correlated with the dielectric characteristics of the oxide

film and by forming the water-soluble species through reactions of Cl^- and OH^- as discussed above. The lowest total R_0 represented by TMAZ was in confirmation with the high transfer coefficient from potentiodynamic polarization (Ref 41) attributed to the dissolution (desorption of soluble metal complexes from the surface) reactions.

Compared to BM and TMAZ, the uniform distribution of relatively fine intermetallic precipitates in the WNZ would possibly produce less disruption in the continuity of passive film. The low ' R_0 ' of BM and TMAZ was due to the formation of micro-galvanic cells at the surface due to cathodic nature of intermetallic phase compared to Al matrix. The additional decrease in total resistance ($R_{ct} + R_0$) by TMAZ could also be related to active nature of the distorted grain structure which was affiliated with the shift in the major diffraction plane from the (111) to (200). This finding suggested that the magnitude of total resistance for electrochemical reactions followed the $\text{WNZ} > \text{BM} > \text{TMAZ}$ sequence.

Figure 8 shows the surface of BM, TMAZ and WNZ after exposure to 3.5% NaCl solution. It can be seen that BM and TMAZ samples were severely corroded in this aggressive medium. The formation of porous and flakes type thick corrosion product on these samples supported the electrochemical results very well [Fig. 8(a), and (b)]. These surface features also validate our hypothesis about the development of local galvanic cells particularly at the surface of TMAZ and BM due to the presence of high concentration of large size CuAl_2 particles (cathodic) in the anodic Al matrix. Furthermore, the surface of WNZ depicted least surface damage due to corrosion under similar conditions as shown in Fig. 8(c) and it was also confirmed electrochemically by its relatively large polarization resistance than BM and TMAZ. The EXD analyses of the BM, TMAZ and WNZ also validated the formation oxide product on

the surface as indicated by the presence of oxygen [Fig. 8(d)]. However, compared to BM and TMAZ, the relatively low oxygen concentration on the WNZ after exposure to saline solution was in confirmation with the electrochemical results as discussed above.

4. Conclusions

1. The higher rotational speed of welding tool induced severe grain distortion and affected distribution of CuAl_2 '0' phase in the TMAZ compared to WNZ where the temperature excursion was sufficiently higher for recrystallization.
2. The strain hardening of grain structure within TMAZ led to a slight increase in yield strength but the low tensile strength and 5% decrease in elongation of the welded sample than BM was attributed to the microstructural inhomogeneity in the TMAZ.
3. The higher charge transfer coefficients (α_a and α_c) measured from the polarization curve of TMAZ corresponded to the defective structure of passive film which could preferentially accelerate charge transfer reactions at the interface of matrix and second phase.
4. The relatively low limiting current response by the WNZ in the regime-II corresponded to the strong adsorption tendency of intermediate species ($\text{H}_2\text{O}_{\text{ads}}$, H_{ads}) within the surface oxide film formed compared to BM and TMAZ.
5. The higher overall corrosion current density of BM compared to TMAZ and WNZ was beneficial in terms of limited galvanic attack at the weld region.
6. The lower resistance to adsorption ' R_0 ' and overall total resistance ($R_{\text{ct}} + R_0$) presented by TMAZ from the impedance spectroscopy was in support with the potentiodynamic polarization results.

Acknowledgments

The authors gratefully acknowledge the technical support provided by Mian Mazhar Maqbool for welding the plate samples under suggested conditions.

References

1. H. Ezuber, A. El-Houd, and F. El-Shawesh, A Study on the Corrosion Behavior of Aluminum Alloys in Seawater, *Mater. Des.*, 2008, **29**(4), p 801–805
2. A.K. Jha, S.N. Murty, V. Diwakar, and K.S. Kumar, Metallurgical Analysis of Cracking in Weldment of Propellant Tank, *Eng. Fail. Anal.*, 2003, **10**(3), p 265–273
3. C. Huang and S. Kou, Partially Melted Zone in Aluminum Welds-Liquation Mechanism and Directional Solidification, *Weld. J. N. Y.*, 2000, **79**(5), p 113-s
4. D.H. Phillips, *Solid-State Welding Processes*, Welding Engineeringed, Wiley, Hoboken, 2016, p 95–113
5. W.M. Thomas, E.D. Nicholas, J.C. Needham, M.G. Murch, P. Temple-Smith, C.J. Dawes, Friction Welding, Google Patents (1995)
6. C. Rhodes, M. Mahoney, W. Bingel, R. Spurling, and C. Bampton, Effects of Friction Stir Welding on Microstructure of 7075 Aluminum, *Scr. Mater.*, 1997, **36**(1), p 69–75
7. G. Liu, L. Murr, C. Niou, J. McClure, and F. Vega, Microstructural Aspects of the Friction-Stir Welding of 6061-T6 Aluminum, *Scr. Mater.*, 1997, **37**(3), p 355–361
8. C. Patil, H. Patil, and H. Patil, Experimental Investigation of Hardness of FSW and TIG joints of Aluminium Alloys of AA7075 and AA6061, *Frattura ed Integrità Strutturale*, 2016, **37**, p 325–332
9. P. Staron, M. Kocak, S. Williams, and A. Wescott, Residual Stress in Friction Stir-Welded Al Sheets, *Phys. B*, 2004, **350**(1), p E491–E493
10. O. Hatamleh, I.V. Rivero, and A. Maredia, Residual Stresses in Friction-Stir-Welded 2195 and 7075 Aluminum Alloys, *Metall. Mater. Trans. A*, 2008, **39**(12), p 2867–2874
11. V. Farajkhah and Y. Liu, Effect of Clamping Area and Welding Speed on the Friction Stir Welding-Induced Residual Stresses, *Int. J. Adv. Manuf. Technol.*, 2017, **90**(1–4), p 339–348
12. D. Wadson, X. Zhou, G. Thompson, P. Skeldon, L.D. Oosterkamp, and G. Scamans, Corrosion Behaviour of Friction Stir Welded AA7108 T79 Aluminium Alloy, *Corros. Sci.*, 2006, **48**(4), p 887–897
13. J. Kang, R.-D. Fu, G.-H. Luan, C.-L. Dong, and M. He, In-Situ Investigation on the Pitting Corrosion Behavior of Friction Stir Welded Joint of AA2024-T3 Aluminium Alloy, *Corros. Sci.*, 2010, **52**(2), p 620–626
14. M. Song and R. Kovacevic, Thermal Modeling of Friction Stir Welding in a Moving Coordinate System and its Validation, *Int. J. Mach. Tools Manuf.*, 2003, **43**(6), p 605–615
15. M. Khandkar, J.A. Khan, and A.P. Reynolds, Prediction of Temperature Distribution and Thermal History during Friction Stir Welding: Input Torque Based Model, *Sci. Technol. Weld. Joining*, 2003, **8**(3), p 165–174
16. J.-Q. Su, T.W. Nelson, and C.J. Sterling, Microstructure Evolution during FSW/FSP of High Strength Aluminum Alloys, *Mater. Sci. Eng., A*, 2005, **405**(1), p 277–286
17. M. Dumont, A. Steuwer, A. Deschamps, M. Peel, and P. Withers, Microstructure Mapping in Friction Stir Welds of 7449 Aluminium Alloy Using SAXS, *Acta Mater.*, 2006, **54**(18), p 4793–4801
18. A.P. Reynolds, Flow Visualization and Simulation in FSW, *Scr. Mater.*, 2008, **58**(5), p 338–342
19. H.N.B. Schmidt, T. Dickerson, and J.H. Hattel, Material Flow in Butt Friction Stir Welds in AA2024-T3, *Acta Mater.*, 2006, **54**(4), p 1199–1209
20. M. Jariyaboon, A. Davenport, R. Ambat, B. Connolly, S. Williams, and D. Price, The Effect of Welding Parameters on the Corrosion Behaviour of Friction Stir Welded AA2024-T351, *Corros. Sci.*, 2007, **49**(2), p 877–909
21. F.A. Ghauri, A. Farooq, A. Ahmad, and K. Deen, Effect of Friction Stir Welding on Microstructure and Corrosion Behavior of LF6 Aluminum Alloy, *Mater. Res. Express*, 2017, **4**(3), p 036501
22. A. Scialpi, M. De Giorgi, L. De Filippis, R. Nobile, and F. Panella, Mechanical Analysis of Ultra-Thin Friction Stir Welding Joined Sheets with Dissimilar and Similar Materials, *Mater. Des.*, 2008, **29**(5), p 928–936
23. H. Liu, Y. Chen, and J. Feng, Effect of Zigzag Line on the Mechanical Properties Of Friction Stir Welded Joints of an Al-Cu Alloy, *Scr. Mater.*, 2006, **55**(3), p 231–234
24. K. Surekha, B. Murty, and K.P. Rao, Effect of Processing Parameters on the Corrosion Behaviour of Friction Stir Processed AA 2219 Aluminum Alloy, *Solid State Sci.*, 2009, **11**(4), p 907–917
25. W. Xu, J. Liu, and H. Zhu, Pitting Corrosion of Friction Stir Welded Aluminum Alloy Thick Plate in Alkaline Chloride Solution, *Electrochim. Acta*, 2010, **55**(8), p 2918–2923
26. E. Bousquet, A. Poulon-Quintin, M. Puiggali, O. Devos, and M. Touzet, Relationship between Microstructure, Microhardness and Corrosion Sensitivity of an AA 2024-T3 Friction Stir Welded Joint, *Corros. Sci.*, 2011, **53**(9), p 3026–3034
27. C.V. Rao, G.M. Reddy, and K.S. Rao, Microstructure and Pitting Corrosion Resistance of AA2219 Al-Cu Alloy Friction Stir Welds-effect of Tool Profile, *Def. Technol.*, 2015, **11**(2), p 123–131
28. M. Janjić, M. Vukčević, V. Mandić, D. Pavletić, and N. Šibalić, Microstructural Evolution during Friction Stir Welding of AlSi1MgMn Alloy, *Metallurgija*, 2012, **51**(1), p 29–33
29. Z. Zhang, B. Xiao, and Z. Ma, Effect of Welding Parameters on Microstructure and Mechanical Properties of Friction Stir Welded 2219Al-T6 Joints, *J. Mater. Sci.*, 2012, **47**(9), p 4075–4086

30. B. Liechty and B. Webb, The Use of Plasticine as an Analog to Explore Material Flow in Friction Stir Welding, *J. Mater. Process. Technol.*, 2007, **184**(1), p 240–250
31. W. Xu, J. Liu, G. Luan, and C. Dong, Temperature Evolution, Microstructure and Mechanical Properties of Friction Stir Welded Thick 2219-O Aluminum Alloy Joints, *Mater. Des.*, 2009, **30**(6), p 1886–1893
32. Y. Chen, H. Liu, and J. Feng, Friction Stir Welding Characteristics of Different Heat-Treated-State 2219 Aluminum Alloy Plates, *Mater. Sci. Eng. A*, 2006, **420**(1), p 21–25
33. H. Liu, H. Fujii, M. Maeda, and K. Nogi, Tensile Properties and Fracture Locations of Friction-Stir-Welded Joints of 2017-T351 Aluminum Alloy, *J. Mater. Process. Technol.*, 2003, **142**(3), p 692–696
34. T. Kobayashi, Strength and Fracture of Aluminum Alloys, *Mater. Sci. Eng. A*, 2000, **280**(1), p 8–16
35. A.W. Thompson, Modeling of Local Strains in Ductile Fracture, *Metall. Mater. Trans. A*, 1987, **18**(11), p 1877–1886
36. M.G. de Chialvo and A. Chialvo, Hydrogen Evolution Reaction: A Kinetic Study on Electrodes with Two Domains of Adsorption Sites, *J. Electroanal. Chem.*, 1995, **388**(1–2), p 215–224
37. G. Burstein, C. Liu, R. Souto, and S. Vines, Origins of Pitting Corrosion, *Corros. Eng. Sci. Technol.*, 2004, **39**(1), p 25–30
38. T. Nguyen and R. Foley, The Chemical Nature of Aluminum Corrosion III. The Dissolution Mechanism of Aluminum Oxide and Aluminum Powder in Various Electrolytes, *J. Electrochem. Soc.*, 1980, **127**(12), p 2563–2566
39. N. Birbilis and R. Buchheit, Electrochemical Characteristics of Intermetallic Phases in Aluminum Alloys an Experimental Survey and Discussion, *J. Electrochem. Soc.*, 2005, **152**(4), p B140–B151
40. Z. Foroulis and M. Thubrikar, On the Kinetics of the Breakdown of Passivity of Preanodized Aluminum by Chloride Ions, *J. Electrochem. Soc.*, 1975, **122**(10), p 1296–1301
41. W. Xu and J. Liu, Microstructure and Pitting Corrosion of Friction Stir Welded Joints in 2219-O Aluminum Alloy Thick Plate, *Corros. Sci.*, 2009, **51**(11), p 2743–2751
42. E. McCafferty, Sequence of Steps in the Pitting of Aluminum by Chloride Ions, *Corros. Sci.*, 2003, **45**(7), p 1421–1438
43. P.B. Srinivasan, K. Arora, W. Dietzel, S. Pandey, and M. Schaper, Characterisation of Microstructure, Mechanical Properties and Corrosion Behaviour of an AA2219 Friction Stir Weldment, *J. Alloy. Compd.*, 2010, **492**(1), p 631–637